Journal of Manufacturing Processes 85 (2023) 246–261

Contents lists available at ScienceDirect

Journal of Manufacturing Processes

journal homepage: www.elsevier.com/locate/manpro

Method for prediction of forming limit height in multistep incremental forming with real-time decision making

Paulo Sergio Olivio Filho [a], Émillyn Ferreira Trevisani Olivio [a], Chetan P. Nikhare [b,*], Pablo Deivid Valle [c], Paulo Victor Prestes Marcondes [c]

[a] *UTFPR - Universidade Tecnológica Federal do Paraná, Brazil*
[b] *Penn State Erie – The Behrend College, Erie, PA, USA*
[c] *UFPR – Universidade Federal do Paraná, Brazil*

ARTICLE INFO

Keywords:
Surface area limit
Incremental forming
Numerical simulation
Ductile damage
Forming limit height

ABSTRACT

The multistep incremental forming is a complex process that requires good control of process parameters to create parts without fractures or cracks. In general, the failure prediction in this process is restricted to experiments and applications in finite element simulations. This paper presents an approach to real-time failure prediction in multistep incremental forming from step-by-step strain analyses. Previous single point incremental forming (SPIF) studies have been applied to BH180GI steel at various thicknesses to obtain data on maximum strain, critical wall angles, and the fracture forming limit line for the material. These data were used as a basis for preventing and predicting failure. The experiments were carried out with steps from 30° to 90° in increments of every 10°, totaling 7 steps achieving higher forming heights. From the angle of 60° onwards, measurements of strain were performed step by step and compared with the fracture forming limit line for each material thickness. When the strain was equal or exceeded the fracture forming limit line and the critical fracture thickness, geometry parts, and path corrections were imposed to minimize local strain ensuring a product without fracture. The results showed that the methodology and the corrections imposed prevented the failure and ensured greater formability of the material. This leads to a minimum thickness of 0.098 mm in the wall of the material, in addition to indicating the presence of a maximum limit of the deformed surface area of the material. This indicated a limit for which it is possible to apply the distribution of strain in the material at different forming heights and radius of the part. For the computer simulations, the mechanical properties, constitutive laws, isotropic hardening and a ductile damage criterion based on fracture forming limit line (FFL) with the fracture energy of the material for failure prediction were applied. These data were fed to the numerical model using an explicit integration approach, with a shell element (S4R) with reduced integration and adequate refining. The simulations in multistep incremental forming were efficient and were able to demonstrate the efficiency of this methodology with the application of corrections in geometry and the path in real-time.

1. Introduction

Many countries are focused on manufacturing simple products, making on large productions as their business goal. In recent years, strong market competitiveness has brought the need for change for new ways of manufacturing products, faster, less costly, better quality, and sustainable production. To achieve all the current needs of manufacturing, companies are strengthening their horizons by making their factories smart, autonomous, flexible, iterative, and independent [1]. Along with these advances, new technologies are being researched and applied to make them viable for the industrial sector. In this context, the studies on the incremental sheet forming process have been growing due to its flexibility and easy application. Its basic concept is completely different from the traditional deep drawing processes. In the incremental forming process, the final geometry is generated by the trajectory of a small and simple tool, which deforms the sheet metal fixed by a clamping tool. The fact of not needing dies, differentiates this process from any other, shortening the waiting time and guaranteeing quick and positive answers in industrial productions due to the flexibility of the process, focus on the customer's product, creation of differentiated

* Corresponding author.
E-mail address: cpn10@psu.edu (C.P. Nikhare).

https://doi.org/10.1016/j.jmapro.2022.11.052
Received 9 June 2022; Received in revised form 1 November 2022; Accepted 16 November 2022
Available online 1 December 2022

products with low industrial costs [2]. This technology requires lower forming force, reducing the size and capacity of machines and equipment, and exhibits higher conformability compared to conventional deep drawing processes, which is related to its type of application and the strain hardening mechanism, which retards the sheet necking that usually occurs in deep drawing processes [3] [4].

In the single point incremental forming (SPIF) process, according to reviews by [5] the choice of optimal process parameters (mainly: tool radius, spindle speed and step down) help to improve the conformability according to the applied path strategy. According to [6], the path strategies applied by the tool in this process can be of the stepped circular type, varying the pass depth; of the alternating circular type, which follows a stepped movement but alternates the initial tool contact position eliminating the scarring generated by the stepped process; and of the helical path type, where the tool follows a downward spiral-shaped path outlining the shape of the part geometry. Depending on the process parameters selected the helical path results in better surface quality and better geometric accuracy [7]. If the surface finish of the part is an important aspect of the process, especially for free-form parts and/or parts with variable wall angles, the path with constant steps is not the best. In this case, the spiral path with a constant radial step can generate better results [8]. Generally, the size of the vertical pass depth is defined by the Dz increment, with typical values between 0.1 mm to 2 mm, with smaller values promoting better strain and surface quality [9]. However, in the SPIF process steep wall angles are impossible to form in a single step. The nature of material strain occurs only in a small area that contacts the tool, and the surrounding material cannot be moved into the strain zone to compensate for the local material insufficiency, and failure occurs.

To overcome this problem, in the multistep incremental forming process (MSIF), if the forming strategy is well designed, a more uniform thickness distribution can be obtained and parts with steeper wall angles can be produced [10]. According to [11] the multistep path for product realization is mainly based on the developer's experience. For [12], the tool paths can be classified into two types, the out-in (OI) and in-out (IO) strategies. The OI process was implemented by [13] with a five-steps strategy for wall angles up to 90°. And the OI and IO process in various configurations (down-down (DD) and down-up (DU)) was analyzed by [10] in a strategy consisting of five stages to form a cylindrical cup, starting with a cone design, and increasing the wall angle with each step without changing the maximum depth of the part [14]. evaluated the stepped path characteristic for creating parts in MSIF. The study reveals that type (OI) and (IO) result in some degree of rigid body motion (RBM), which is reduced if the yield stress or sheet thickness increases. To improve geometric accuracy [15] presented three strategies for application in MSIF, in their study the third strategy proved more advantages, which consists of forming a cone or pyramid at a lower wall angle and initial height than the final part, and in subsequent steps, the cone wall angle and forming height is gradually increased until the final step. This strategy generated lower RBM and less shape deviation. The concept applied by [10,14] was extended and improved into a mixed OI and IO path strategy to compensate for RBM elaborated by [16]. Although there are several possible strategies, easily computationally applicable paths are still the most widely used, in agreement with works by [17,18] applying DDDD-type (down-down-down-down) OI strategies as reported by [10]. In work of [19] on MSIF, reports that the strain is minimized with the number of intermediates steps up to the maximum wall angle formed. Due to the number of subsequent steps in the process, the tool path, forming parameters, and effects such as rigid body movement, geometric accuracy, conformability, and improved thickness distribution play a vital role during product development.

Therefore, to evaluate and optimize the tool path, analyze the thickness distribution at different parameters and predict the fracture, applications using finite element method (FEM) are commonly used to promote better decision making. The process presents a large local plastic strain gradient, in a region much smaller than the blank area, so for a good discretization generated by FEM, a very fine mesh is required, which generates a large central processing unit (CPU) processing time. For this purpose, integration models explicit and implicit have been tested by researchers in different simulation cases. The implicit method uses an iterative and more stable procedure, although it usually has convergence problems for a large number of elements in addition to increasing computational time [20]. The explicit method, on the other hand, is fast, easy to parallelize, easy to achieve convergence, and stable under certain modeling conditions [21]. The researchers [22] presented an FEA using an explicit scheme to investigate the wall angle limitation and the occurrence of geometric deviations. To study the failure, the Gurson-Tveergard Needleman (GTN) model of ductile damage was implemented to study the influence of tool radius and vertical pitch on damage evolution in the incremental sheet forming (ISF). The data were close to the experimental ones and the damage evolution qualitatively confirmed that higher forming limits can be achieved with smaller tools. The work of [23] presented simulations using an explicit dynamic method on different tool paths to test the effect of the path on the strain of the sheet and reduce the time by the implicit method. The use of standard/implicit method with the shell- (code lagamine) and block-type elements and concluded after several studies that the use of block elements with isotropic von Mises/Voce hardening generated better approximations with the experimental strength data [24]. The shape accuracy at different strain paths were studied in [25]. The simulations were performed using dynamic code in LS-DYNA software, and the result showed satisfactory. A mesh defined by 8 layers of 3D solid elements coupled with a damage model to predict fracture in SPIF were performed with LS-Dyna explicit code [26]. The model was validated and used in 70° wall angle cone tests and a funnel-type cone. The results presented data on damage accumulation, thickness, fracture, and the effects of bending on fracture [27]. studied different damage models for application to different parts in SPIF via Abaqus/Explicit. The result showed a low error percentage with good approximations. A mixed (isotropic/kinematic) hardening model was used with a VUMAT subroutine in Abaqus/Explicit to validate the model and predict the damage evolution in the plate [28]. The simulation results were compared with experimental data and applied to the SPIF process revealing the effect of triaxiality.

However, although many efforts have been made in toolpath studies to improve geometric accuracy and thickness uniformity in the multistep incremental forming (MSIF), there is no approach for failure prediction, being left to trial-and-error experimental studies or FEM simulations, which, according to [29], is very time-consuming, preventing rapid product creation. In this sense, focusing on establishing the forming limit and predicting failures in MSIF, to ensure greater gains in productivity, competitiveness, speed in part creation and stability in the process, this paper discusses a methodology for real-time analysis, step by step, analyzing the strain and proposing toolpath adjustments and minor changes in part geometry, to ensure the integrity of the final product without the occurrence of failures. This innovative methodology proposes to determine the forming limit height for cylindrical cup parts at different radius of curvature of the part, which can also be correlated with the maximum deformed surface area of the blank without fracture.

2. Materials

In this study, sheets of low-carbon, thin-gauge steels with good conformability at room temperature were used. The material used in the multistep incremental forming was cold-rolled BH180GI steel with galvanized coating, in thicknesses of 0.43 mm and 0.8 mm. For material characterization, chemical composition analyses of the uncoated substrate were performed with the TASMAN Q4 optical emission spectrometer, shown in Table 1.

The mechanical properties of the material were obtained with the WDW-100E equipment employing a strain gauge attached to the

Table 1
Chemical compositions of BH 180 GI steel.

% C	% Mn	% P	% S	% Si	% Nb	% Cu	% B	% Al	% Fe
0.03	0.378	0.0321	0.02	0.026	0.018	0.012	0.007	0.054	99.423

specimens in the rolling directions (R.D.) of 0°, 45°, and 90°, with the speed set at 0.02 mm/min, according to the standard type 1 of NBR ISO 6892-1:2013. The averages of the mechanical properties of the material are presented in Table 2.

The anisotropic properties of the materials were measured according to ASTM E-517 and the normal anisotropy coefficient (*r*) and the planar anisotropy coefficient (Δr) were calculated from the averages of the anisotropy coefficient in each rolling direction (r0, r45, r90). The average data are presented in Table 3.

Because the material has a yield plateau, for the plastic region of the curve in the strain range $\varepsilon < 0.1$ a polynomial approximation was used, and for the strain range $\varepsilon > 0.1$, the power-law was applied. Each of the equations for the experimental curve over the entire strain range was obtained by the method of least squares. However, the transition region and the large strain plastic regions were combined without significant degradation, with $R^2 > 0.95$. For 0.43 mm thick steel sheet, Eqs. (1) and (2) were joined and presented the average true stress shown in Fig. 1. Fig. 2 shows the average true stress for 0.8 mm thick steel sheet using Eqs. (3) and (4).

$$\sigma = 226.865\varepsilon^3 - 33.632\varepsilon^2 + 4917.005\varepsilon - 21577.057, \text{ for } \varepsilon < 0.1 \tag{1}$$

$$\sigma = 453.296\varepsilon^{0.267}, \text{ for } 0.1 < \varepsilon < 0.39 \tag{2}$$

$$\sigma = 325.734\varepsilon^3 + 534.737\varepsilon^2 - 6204.801\varepsilon + 46382.831 \text{ for } \varepsilon < 0.1 \tag{3}$$

$$\sigma = 461.831\varepsilon^{0.258} \text{ for } 0.1 < \varepsilon < 0.39 \tag{4}$$

3. Experimental tests

For the experimental tests a ROMI D600 CNC machining center (Fig. 3a) was used; an ISF device made of heat-treated SAE 4140 steel was used to fix the specimens (Fig. 3b). This device is composed of a base and a clamping fixture. The base of the device is fixed to a lathe chuck, which is then fixed by screws on a sheet adapted for locking the machining center table, giving the device rigidity and reliability. As a tool, a stainless-steel extension rod and a High-speed steel round bar punch were used, with a TiAlCN (titanium aluminum carbonitride) coating, made by PVD (Physical Vapor Deposition). The hardness of the coating is in the order of 2600 HV (Fig. 3d). For the experiments, specimens with dimensions 70 × 70mm were cut, with a diameter of 50 mm useful for incremental forming, and the rest of the sheet between 50 mm and 70 mm was used for attachment to the device (Fig. 3c). For strain study, a 2 mm square mesh was created and printed on the sheet. Measurement of the deformation and thickness on the sheet during the MSIF process was performed using an Olympus BX53 microscope and a millesimal scale digital thickness gauge.

The tool path has a significant effect on dimensional accuracy, surface roughness, processing time, and thickness variation. In this work, a staggering path of the DDDD out-in type was applied in agreement with [14], with a sequence starting from smaller cones to larger cones [15]. The use of CAD/CAM software was required to perform the tool paths, and a post-processor was configured to generate the numerical code in NC and APT format for machine and FEM applications.

Table 2
Mechanical proprieties of BH 180 GI steel.

Parameters	0.43 mm	0.8 mm
E - Modulus of Elasticity (MPa)	210,000	210,000
υ - Poisson's ratio	0.33	0.33
ρ - Density (g/cm^3)	7.87	7.87
US – Ultimate Strength (MPa)	244.490	255.572
YS – Yield Strength (MPa)	220.101	219.162
EL - Elongation A50 (%)	45.179	47.413

Table 3
Normal and planar anisotropy of the material.

Material	Thickness (mm)	*r*0	*r*45	*r*90	*r*	Δr
BH 180 GI	0.43	0.964	0.996	0.992	0.987	−0.018
BH 180 GI	0.8	1.182	0.973	1.046	1.043	0.141

All experimental tests were performed with abundant lubrication of Lubrax GL 5 90 mineral oil on the part placed manually, keeping the tool/part contact region immersed in oil.

For experiments, the sought parameters that would improve the conformability of the material, with the use of low tool diameter and step down and spindle speed [5], thus, a tool of radius (Rf) 4 mm, step down (Dz) of 0.2 mm and spindle speed of 600 RPM was used. Initial studies in SPIF and MSIF showed that the use of feed rate at 150 mm/min improved conformability and delayed fracture at wall angles greater than or near critical angles in agreement with [30–32]. The MSIF process was performed in 7 steps, starting at the 30° angle up to 90° with a jump every 10° with a feed rate of 600 mm/min up to 60° angles and a feed rate of 150 mm/min for higher angles. The experiments, were fixed, forming heights of 11 mm, 13 mm, 15 mm, and 17 mm for the 0.43 mm thick sheet, and forming heights of 11 mm, 13 mm, 15 mm, 17 mm, and 19 mm for the 0.8 mm thick sheet. The experimental design is presented in Table 4.

From the forming heights, the intermediate geometries and the step-by-step forming path were established as shown in Fig. 4 for the experiments in Table 4.

3.1. Real-time failure analysis methodology

For the product failure study at MSIF, the experimental FFLs were obtained from previous tests at SPIF, generating cones of various wall angles from 30° to 90°. The minimum sheet thickness, average fracture thickness, and plane strain data on the sheet metal were stored for each test. The thickness data were important to establish the critical thickness region, the region where there is maximum strain and minimum thickness without failure. In addition to this region, thicknesses measured in the failure region helped to establish the fracture thickness region for the materials (later presented in Figs. 9 and 11). The plane strain data in the sheet was used to generate the experimental FFL functions at the two sheet thicknesses analyzed. Since ε1 strains are larger, and ε2 strains are smaller in the SPIF experiments, the FFL was extrapolated to larger ε2 strains for the MSIF studies. During the MSIF experiments, to avoid premature product failure, starting at the 60° wall angle, the largest strains (ε1 and ε2) and the smaller thickness located on the surface of the part were measured. These data were stored and compared with the FFL and the critical thickness region obtained in the SPIF experiments. At each pass angle, in plane strain data (ε1 and ε2) and thickness were measured, and when equal or exceeded the limits of experimental FFL and the critical thickness region, changes to the part radius and toolpath were imposed to minimize local stretching.

4. Numerical simulation

The ABAQUS® 6.12.11 software was used in the simulation. To

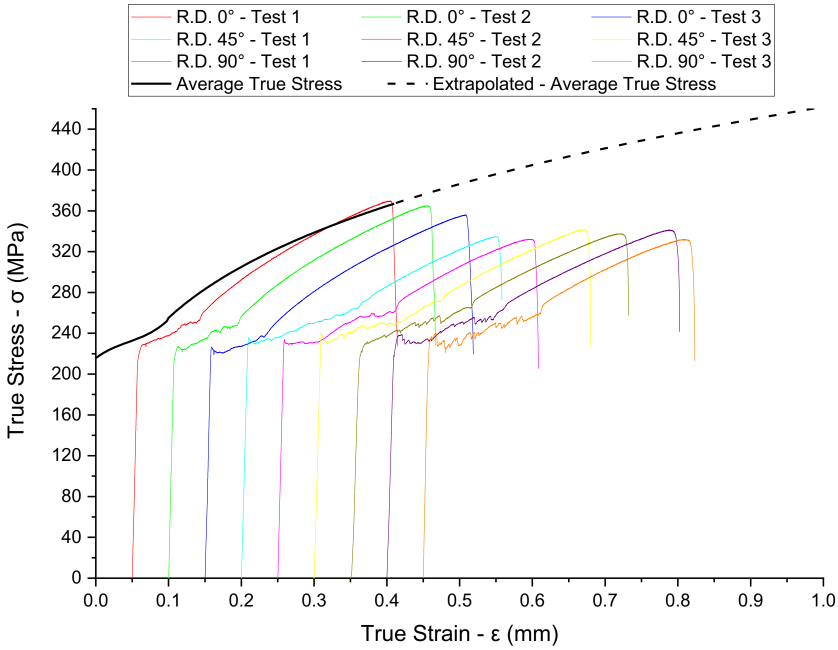

Fig. 1. Tensile true stress-strain for sheet metal thickness 0.43 mm.

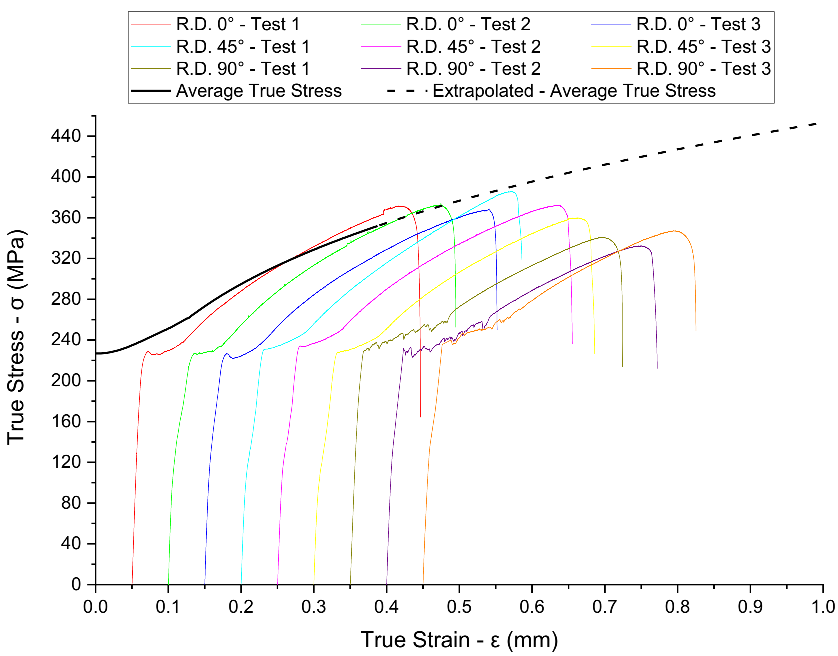

Fig. 2. Tensile true stress-strain for sheet metal thickness 0.8 mm.

approximate the experimental tests performed, a similar model applied by [33] was used in this work (Fig. 5). For simulations, the explicit integration method and application of a shell type element S4R with 9 integration points along with the thickness of the sheet by the standard integration method of the application were used. 7 to 15 number of integration points (NIP) proved adequate in the study [34]. The integration points of 3, 5, 7, 9, 15, 25 and 31 during sheet forming simulation were studied [35] and showed that the results are stabilized at around 5 and 7 NIPs. In summary, 3 integration points are not enough, 5 integration points are the minimum acceptable and 7 integration points can provide the best solution - increasing the number of integration points also increases the CPU time.

The true stress-strain data were assigned to the model together with the isotropic hardening of the Voce/Swift material from the data of [36] after the cyclic test of similar material. (Eqs. (5) and (6)). The Voce/Swift model was implemented to simulate the change of the equivalent stress during the promoted springback by the process after the tool passes.

$$\sigma = \sigma_0 + Q_\infty\left(1 - exp^{-b*\bar{\varepsilon}^{pl}}\right) \tag{5}$$

$$\sigma = \sigma_0 + 131.63\left(1 - exp^{-15.14*\bar{\varepsilon}^{pl}}\right) \tag{6}$$

where, σ_0 is yield stress at zero plastic strain; Q_∞ is the maximum change in the size of the yield surface; b defines the rate at which the size of the

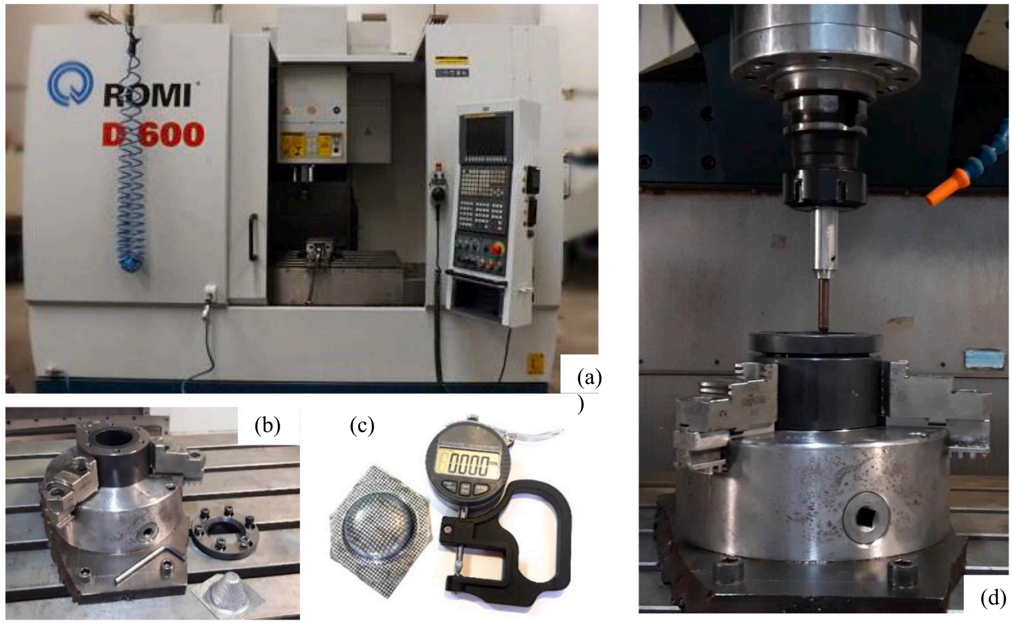

Fig. 3. (a) ROMI D600 machining center; (b) ISF device; (c) specimen and thickness gauge; (d) Forming tool and ISF device attached to the machining center table.

Table 4
Experimental design in multistep incremental forming.

Experiments	Angle (°)	Thickness (mm)	Feed Rate (mm/min)	Rf (mm)	Dz (mm)
A11	30-40-50-60-70-80-90	0.43	600/150	4	0.2
A13	30-40-50-60-70-80-90	0.43	600/150	4	0.2
A15	30-40-50-60-70-80-90	0.43	600/150	4	0.2
A17	30-40-50-60-70-80-90	0.43	600/150	4	0.2
B11	30-40-50-60-70-80-90	0.8	600/150	4	0.2
B13	30-40-50-60-70-80-90	0.8	600/150	4	0.2
B15	30-40-50-60-70-80-90	0.8	600/150	4	0.2
B17	30-40-50-60-70-80-90	0.8	600/150	4	0.2
B19	30-40-50-60-70-80-90	0.8	600/150	4	0.2

yield surface changes as plastic straining develops and $\bar{\varepsilon}^{pl}$ equivalent plastic strain.

The sheet was drawn according to the physical experiment and modeled as a deformable element, and the tool and die were modeled as a rigid analytical body (Fig. 5).

Because the friction between the tool and the sheet metal is unknown, for the studies, it was used the coefficient of friction according to

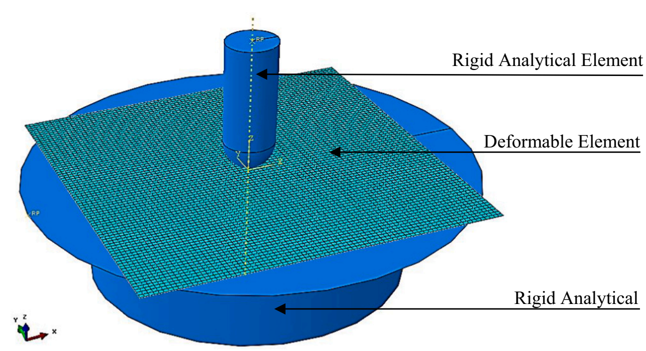

Fig. 5. Model for computer simulation in MSIF.

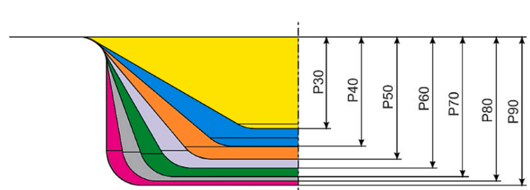

	A11	B11	A13	B13	A15	B15	A17	B17	B19
P30 (mm)	8.5	8.5	9.25	9.25	10	10	10.5	10.5	11
P40 (mm)	9.5	9.5	10.5	10.5	11.75	11.75	12.5	12.5	13.25
P50 (mm)	10	10	11.5	11.5	13	13	14	14	15.25
P60 (mm)	10.25	10.25	12	12	13.75	13.75	15	15	16.5
P70 (mm)	10.5	10.5	12.5	12.5	14.25	14.25	16	16	17.75
P80 (mm)	10.75	10.75	12.75	12.75	14.75	14.75	16.5	16.5	18.5
P90 (mm)	11	11	13	13	15	15	17	17	19

Fig. 4. Geometries of the multistep incremental forming process.

Coulomb's Law with a value of 0.2 according to the work of [37] and studies on similar material conducted by [38]. The friction value was formulated using the penalty method assuming an isotropic directionality.

From the experimental trajectory, the CAM-generated trajectory was converted to cartesian coordinates from the APT extension file, for application via Abaqus® CAE.

To analyze the simulated failure prediction in the process, the ductile damage model was applied. This initiation criterion of ductile damage is a model for predicting damage initiation due to nucleation, growth, and coalescence of voids in ductile metals. The model assumes that the equivalent plastic stress at damage initiation is a function of the stress triaxiality and the strain rate. As input data, the FFL of the material was added, generated from the strain data measured in the previous physical experiments in single-point incremental forming (SPIF). In addition, an average of the fracture energy values calculated by Eq. (7) from the tensile test data was added to the software. The average fracture energy obtained was 20.788 MPa for the 0.43 mm thick sheet and 22.257 MPa for the 0.8 mm thick sheet.

$$G_f = \int_{\overline{\varepsilon}_0^{pl}}^{\overline{\varepsilon}_f^{pl}} L(\sigma_u)\, d\overline{\varepsilon}^{pl} \tag{7}$$

where, G_f is the fracture energy; L is the length of the global mesh element; σ_u is the strength stress of the material and $\overline{\varepsilon}^{pl}$ equivalent plastic strain [39].

4.1. Global mesh size

For the selection of the global mesh size (GMS) or mesh refinement to be considered efficient in this work, equivalent strain data at mesh density 0.7, 0.5 and 0.3 were evaluated on SPIF in truncated cone parts at the 60° wall angles for both sheet thicknesses. Equivalent strain data was taken from a mesh line on the cone wall to create the comparison plots. As presented in Fig. 6a–b, little change in the equivalent strain data along the stamping height was observed. The 0.7 global mesh size model showed 6231 number of elements and an average processing time of 17.34 h. The 0.5 global mesh size model had 12,100 element numbers and an average processing time of 45.31 h. The 0.3 global mesh size model had 22,489 number of elements and an average processing time of 214.617 h.

Although higher refinement can lead to better data, for MSIF studies computational time is a concern, which can range from simulation days to simulation weeks. Thus, based on the refinement data studied and in accordance with [31], the selected mesh density was a global mesh size of 0.7, combining good results and lower computational time for both sheet thicknesses.

5. Results and discussions

Following the methodology, the experiments were performed with no occurrence of fracture. Fig. 7 shows the results for experiments A11 to A17.

Fig. 8 shows the results for experiments B11 to B19. As expected, in thicker sheets, the corrections due to larger strains and thinning occurred later. In experiment B19 the appearance of rigid-body displacement was more pronounced.

Table 5 shows the changes made to the part radius at each wall angle and step, starting at the 60° angle. Experiments A11 to A17, because it is a thinner sheet, presented a greater need for corrections to geometry and toolpath. Experiment A11 did not need any corrections. The corrections started from experiment A13 with increasing change until experiment A17 with a corrected radius of 12 mm. The experiments performed with the thicker sheet showed little correction. From experiment B11 to B19, corrections were only necessary for experiment B19.

Based on the strain measurements made in the plane of the sheet, in experiment A11 there was no need for corrections because the strain did not exceed the fracture limit curve, in the following experiments it was necessary to apply corrections. In experiment A13 the radius of the part was changed to 6 mm for steps larger than 80°. In experiment A15 the correction occurred after the 70° step, the radius was changed to 6 mm, and after, again another correction for subsequent passes with a change of the radius to 8 mm. In experiment A17, the most critical forming for this sheet thickness, the correction occurred after the 70° step, the wall formation and thinning were so great that larger corrections based on the strains measured in the previous tests were applied. The correction was applied with a 10 mm radius, and then again, another correction for subsequent passes with a change in radius to 12 mm for 90°. Fig. 9 demonstrates the growth of the greater strain over the steps.

Fig. 10 shows the maximum thinning found in the part after each step. As it is possible to observe, similarly to the biaxial strain, the final thickness exceeded the critical region of thinning, and the average value of thinning was close to the fracture region reported in the SPIF tests. At the heights that the corrections occurred, it is possible to observe a

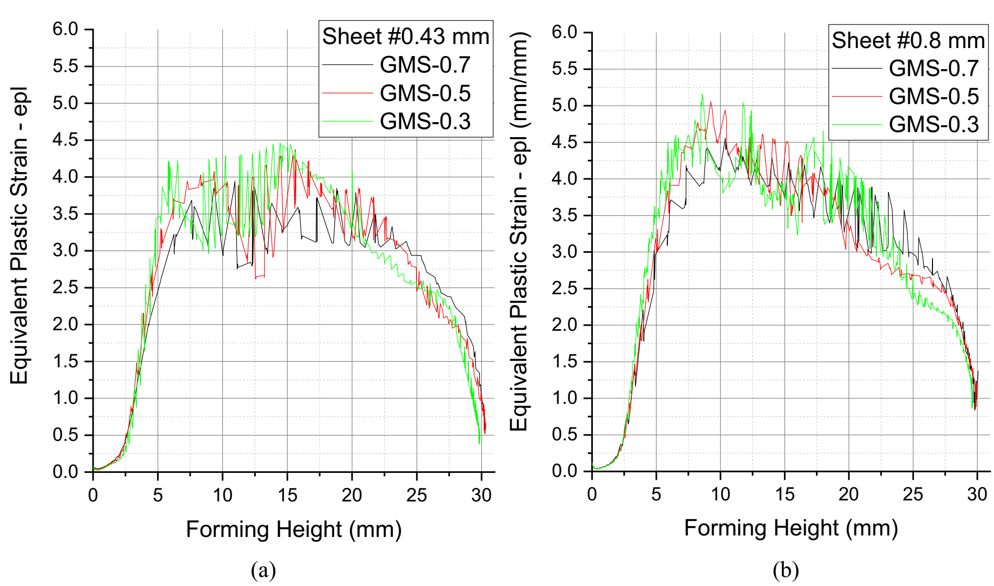

Fig. 6. Global mesh size studies. a) thickness 0.43 mm, b) thickness 0.8 mm.

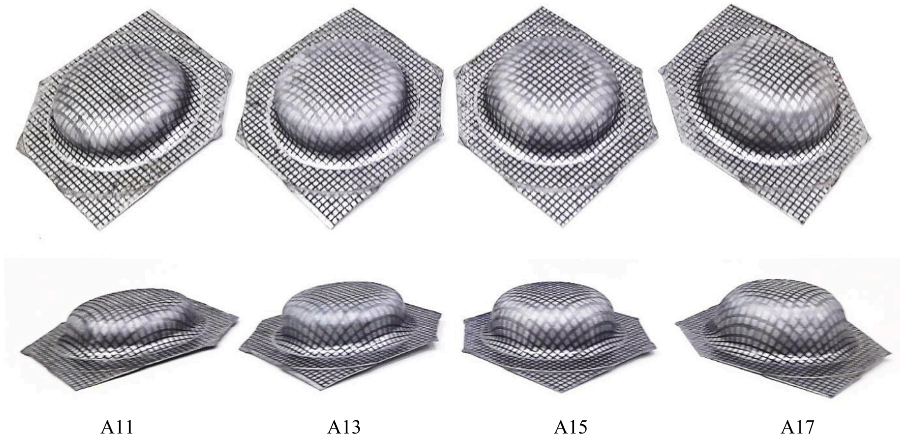

Fig. 7. Multistep experiments in 0.43 mm thick sheet metal.

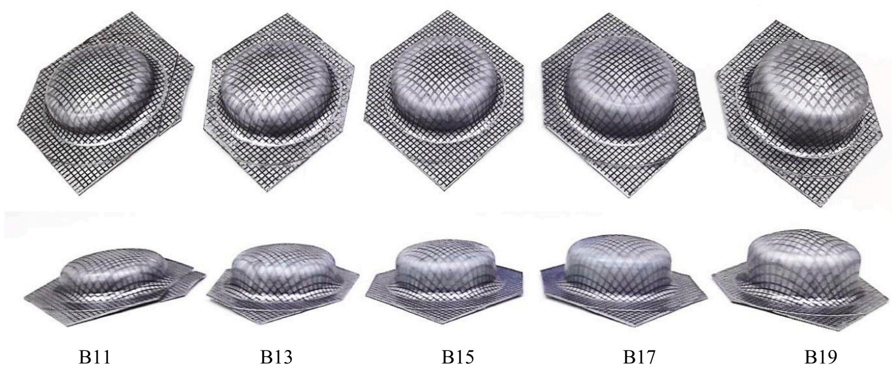

Fig. 8. Multistep experiments in 0.8 mm thick sheet metal.

Table 5
Corrections generated in the radius of the part.

Experiments	Wall angle (°)	R_{60} (mm)	Wall angle (°)	R_{70} (mm)	Wall angle (°)	R_{80} (mm)	Wall angle (°)	R_{90} (mm)
A11	60	4	70	4	80	4	90	4
A13	60	4	70	4	80	4	90	6
A15	60	4	70	4	80	6	90	8
A17	60	4	70	4	80	10	90	12
B11	60	4	70	4	80	4	90	4
B13	60	4	70	4	80	4	90	4
B15	60	4	70	4	80	4	90	4
B17	60	4	70	4	80	4	90	4
B19	60	4	70	4	80	4	90	6

reduction in the thinning rate, which was most evident in experiment A15. In experiment A17 it is possible to observe that at angles of 80° and 90° the thinning was so severe that it exceeded the fracture limit thickness obtained in SPIF. However, it can be concluded that the applied process parameters helped to ensure a quality part with a minimum final thickness of 0.099 mm, without fracture.

In the experiments performed with the thicker sheet, in experiments B11 through B17 there was no need to perform corrections because the strains did not exceed the FFL and the critical thickness. In the next experiment, experiment B19, it was necessary to apply correction to the geometry and tool path, changing the radius of the part to 6 mm. Fig. 11 shows the growth of greater strain along with the passes.

In Fig. 12 the thinning generated in the process was more controlled. In the biaxial strain, only in experiments B17 and B19 did the thinning exceed the critical region found in previous SPIF experiments. In experiment B19 the radius of the part was corrected to 6 mm, which greatly reduced the rate of thinning on the surface of the part. From these experiments, it can be concluded that the process parameters and strain-based corrections helped to ensure a quality part with controlled thickness.

Based on the tests performed and the corrections applied in real-time, we can conclude that the biaxial strain measurements and the use of the FFL as an input parameter for process corrections along the passes helped to ensure fracture-free parts. The interactive analysis procedure together with the strain data from the experiments stored later provided better corrections to produce the following parts, exemplified in experiment A17 performed after experiment A15, which required more expressive corrections.

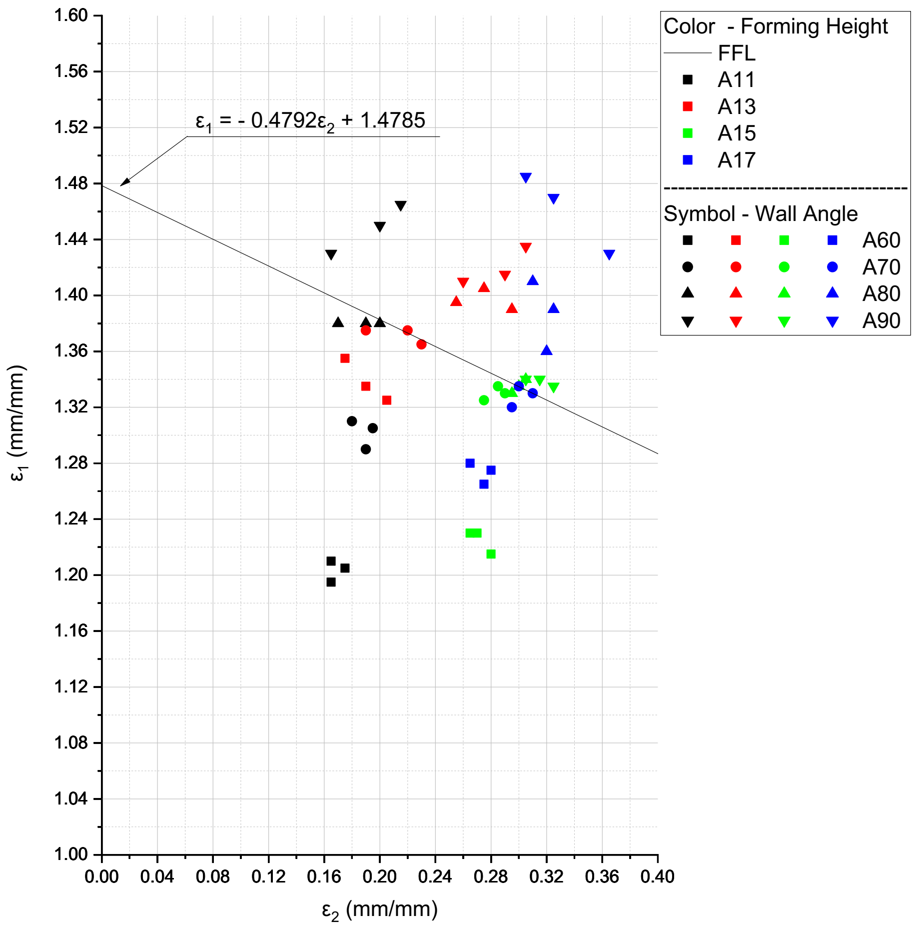

Fig. 9. Biaxial strain in experiments A11 to A17.

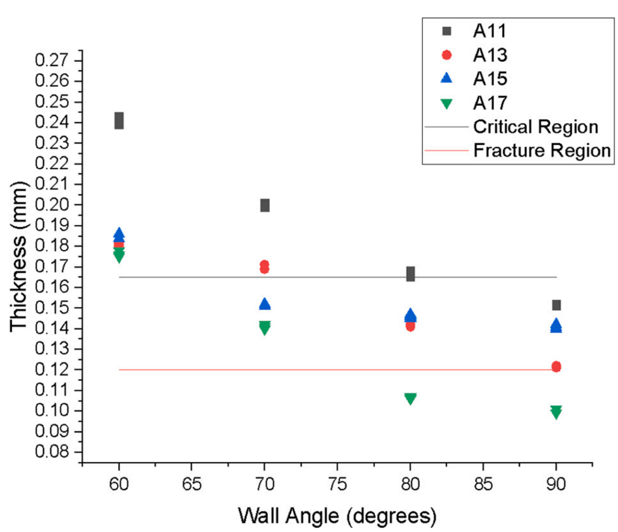

Fig. 10. Thinning in experiments A11 to A17.

5.1. Analysis of deformable surface area in multistep incremental forming

The measured strains and the corrections applied to the geometry and tool path gave satisfactory results, which proved the need for real-time corrections to reduce the strain rate. Based on the paths created a relationship between the deformable surface area in the MSIF process and the estimated deformable surface area of the blank was analyzed.

In Fig. 13, a schematic drawing is presented showing in gray the undeformed region that is located at the top edge and in the central region of the blanking. The region in orange is the deformed surface area in MSIF (DAS_MS). The region in yellow is the area estimated as the deformable blanking surface area (DSA_BL). In both images, the central undeformed area is of the same size.

Fig. 14 shows the plot of deformed surface area in MSIF for tests A11 to A17, at forming wall angles of 60°, 70°, 80°, and 90°. The graph shows that with the increased height in MSIF, the geometry and tool path corrections led to stagnation of the DSA_MS at the maximum value of 3257 mm^2, which generated great thinning in the sample. Through the image, it is verified that with the increase in DSA_MS, there was also an increase in the thinning of the sheet, leading to the understanding that by controlling the surface area one can control the strain. In experiment A11, the 4 mm radius was applied up to the 90° wall angle. It is possible to verify that with the increase of the forming height the same radius could only be applied at smaller angles. As an example, there is experiment A13, 4 mm radius at 80° wall angles, and experiment A15, 4 mm radius at 70° wall angles. The surface area is 2852 mm^2 for experiment A11, 2975 mm^2 for experiment A13, and 2972 mm^2 for experiment A15. The maximum variation of 123 mm^2 in surface area is equivalent to a gain of only 0.9 mm in forming height.

In Fig. 15 the graph of deformed surface area in MSIF is presented for the tests from B11 to B19, at the forming wall angles of 60°, 70°, 80°, and 90°. As it was observed in the thinner sheet, the graph also shows that with the increase in height in MSIF, the geometry and tool path correction led to a DSA_MS of 3991 mm^2, with a correction for the radius of 6 mm. In experiment B17, the 4 mm radius was applied up to the 90° wall angle. With increasing forming height, the same radius could only

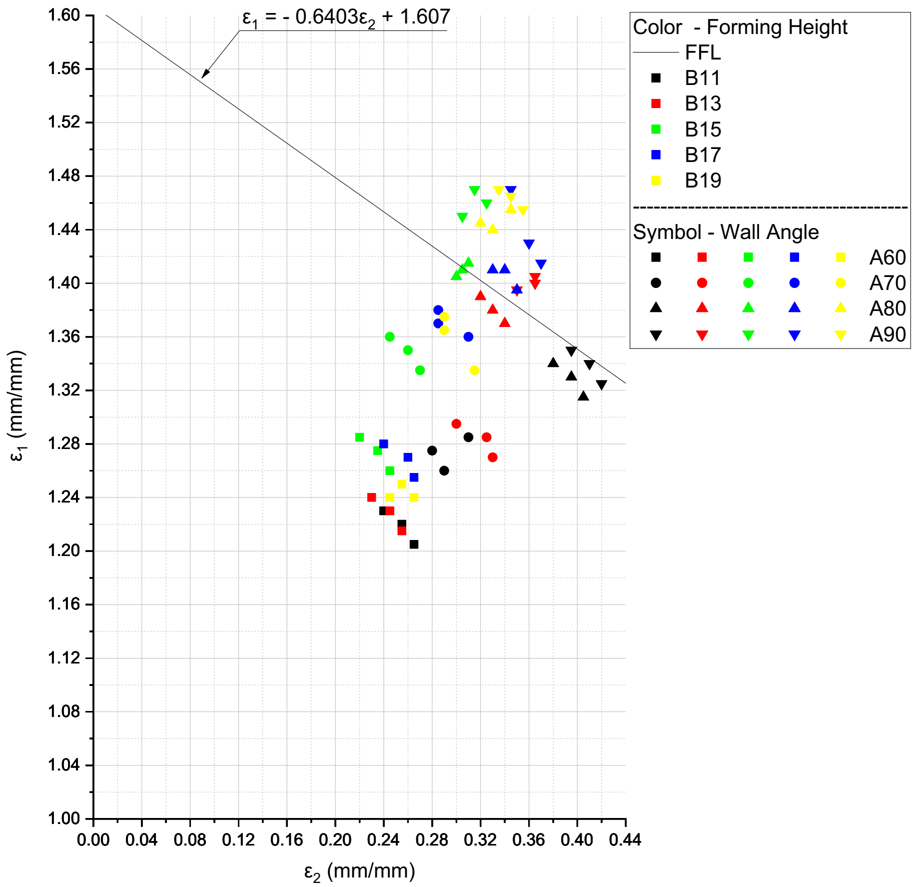

Fig. 11. Biaxial strain in experiments B11 to B19.

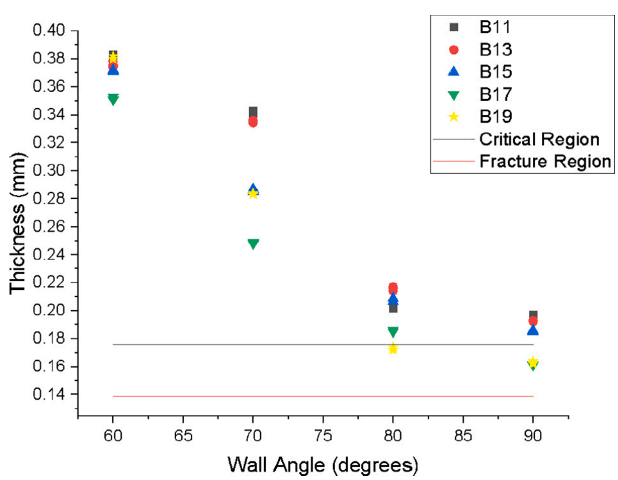

Fig. 12. Thinning in experiments B11 to B19.

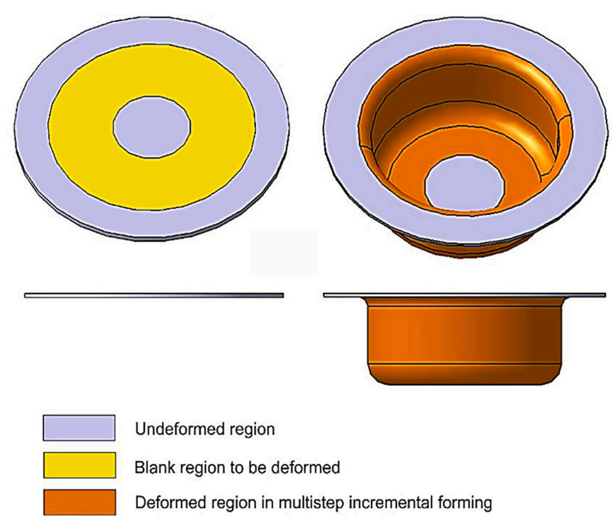

Fig. 13. Undeformed region, blank region, and deformed region in multistep incremental forming.

be applied at smaller angles, as shown in experiment B19 i.e., 4 mm radius at 80° wall angle. The surface area is 3612 mm^2 for B19 and 3789 mm^2 for B17. The maximum variation of 177 mm^2 in surface area, is equivalent to a gain of 1.3 mm in forming height.

As in the tests, there was a small variation in the blanking surface area, which promoted a better distribution of the strain along with the passes, an analysis between the ratio of DSA_MS and DSA_BL, can help to better understand the limits of multistep incremental forming.

Fig. 16 shows the graph of the ratio of DSA_MS by DSA_BL for tests A11 to A17. As observed in the graph the heights are related to the wall angles according to Fig. 6. The graph shows that the forming surface ratio for a 4 mm radius part is between 1.60 and 1.67, on average the ratio obtained for the experiments A11, A13, A15, and A17 with a 4 mm radius is 1.637. Knowing this data, it is possible to define the forming height for any angle >65° with this radius and apply it to any other larger radius for the part. Looking at the ratios of radius 4 mm, where the possible fracture is shown, it is observed that from a height of 11 mm onwards it would not be possible to apply this radius, since the ratio for possible failure in experiments A13 and A15 averaged 1.723, and with

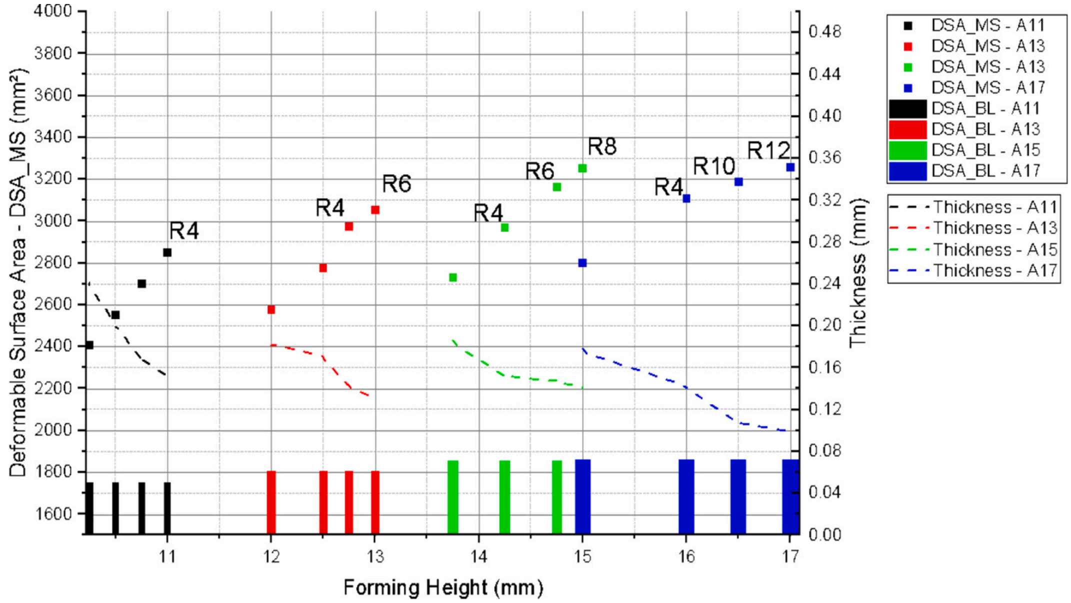

Fig. 14. Deformed surface area by forming height for experiments A11 to A17.

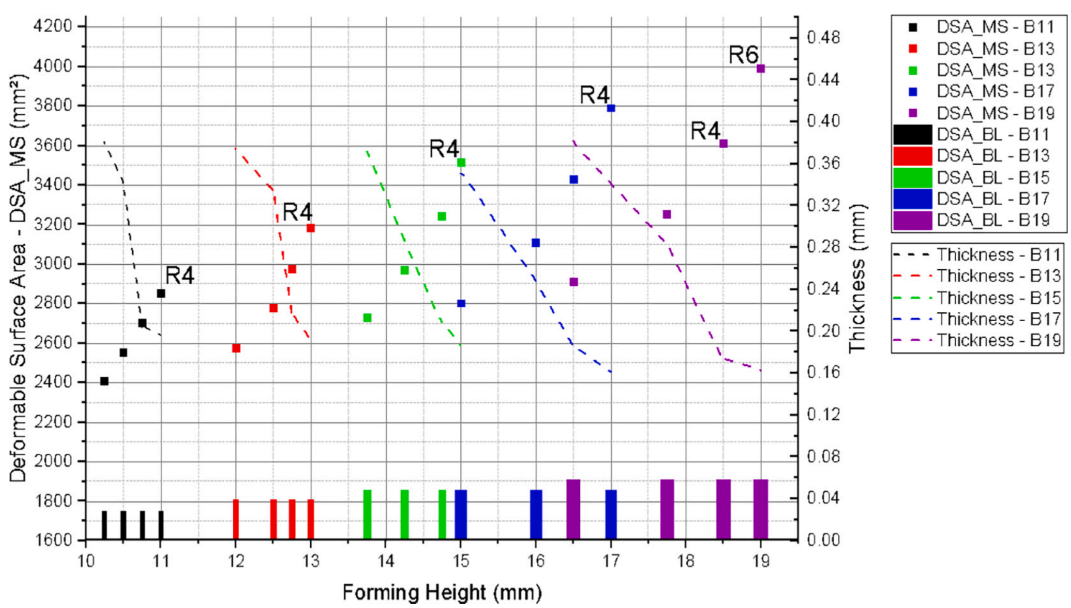

Fig. 15. Deformed surface area by forming height for experiments B11 to B19.

the increase of the forming height, the maximum ratio for experiment A17 with radius 12 mm was equal to 1.753, higher than the previous ones. For the forming surface ratios, it is observed that in experiment A11 a more linear growth tends to the strain limit, while in the other experiments a small decline to the right is presented, which leads to understanding the need to properly distribute the strain and know the forming limits at the beginning of the studies to produce the product.

Fig. 17 shows the graph of the ratio between DSA_MS and DSA_BL for tests B11 to B19. As observed in the graph, the heights are related to the wall angles as shown in Fig. 6. The graph shows a maximum forming surface area ratio of 2.039 (experiment B17), for the use of the 4 mm radius, which is impossible for realizing parts with the thinner sheet. Based on the results of the experiments with the thinner sheet, in experiments B17 and B19 it can be concluded that the best forming surface ratio is between 2.039 and 2.088, on average 2.064. Regarding the forming surface ratios, in experiments B11 to B17, there is an expressive growth of the forming surface ratio, tending to the strain limit. In experiment B19 the growth of the forming surface ratio is minimized through imposed corrections, reducing deformation in the region, and ensuring product integrity.

From the surface area analyses, it can be concluded that the tests applied with measurement and correction in real time helped to establish the limits of multistep incremental forming. Concerning the deformed surface area and the analyzed DSA_MS and DSA_BL forming surface ratio, it is possible to define the initial process parameters based on the forming height and the best corrections to be applied to the part radius to ensure greater reduction of local deformation during MSIF manufacturing. Based on this data presented a DSA_MS to DAS_BL forming surface ratio of 1.637 was established for use on a 0.43 mm thick sheet and 2.064 for use on a 0.8 mm thick sheet.

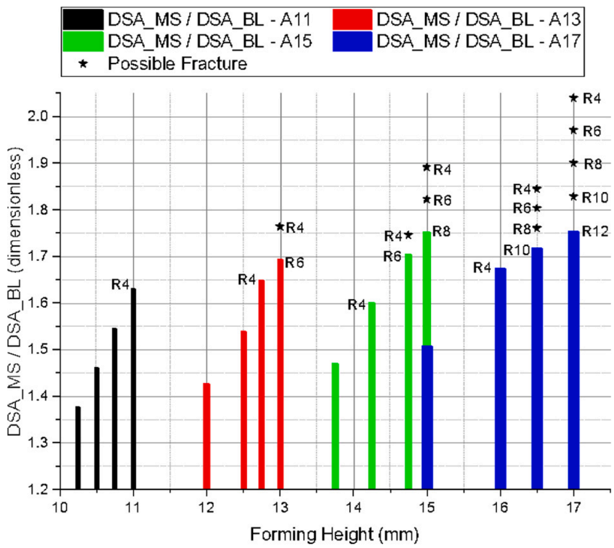

Fig. 16. Forming surface ratio between DSA_MP/DAS_BL for experiments A11 to A17.

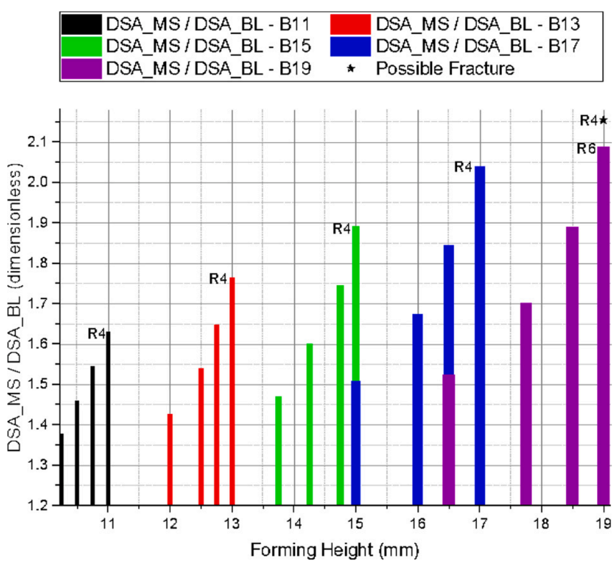

Fig. 17. Forming surface ratio between DSA_MP/DAS_BL for experiments B11 to B17.

5.2. Computer simulation in multistep incremental forming

According to the model described in Fig. 4, the simulations were performed in MSIF for comparison and prediction purposes. To feed the data into the software, the mechanical properties of the materials and mesh and friction parameters, described in topic 4, were used. To analyze the results of the computational model and the fracture prediction, the ductile damage evolution method was applied based on the FFL generated from the previous data measured in the SPIF experiments. The image of the experiments performed for plate 0.43 mm and for plate 0.8 mm are presented in Figs. 18 and 19. Fig. 18 shows that the simulation like what occurred in the practical experiments without the appearance of failure for experiments A11, A13, A15, and A17. The contour values shown in the figures represent the difference in thickness on the surface of the part, explaining clearly deformed and undeformed area. The energy value applied to the ductile damage mechanism was efficient in predicting the fracture, only for experiment A17 - R4, without applying correction, where the fracture nucleated at the 80° wall angle. In the experiment A13 - R4, without the application of correction, the failure did not occur, this may be related to the slope of the FFL curve extrapolated from the experiments in SPIF, as can be seen in Fig. 19, where the strains were below the FFL. In Fig. 19 like what happened with the thinner plate, the correction data were efficient for experiments B11, B13, B15, B17, and B19, preventing the possible fracture of the material. The energy value applied to the ductile damage mechanism helped to identify a possible failure in experiment B19 - R4 if the correction was not applied to the geometry.

From the material properties data applied to the simulations in MSIF, the biaxial strain responses had similar behavior to the strains performed in the practical experiment. The strain ε1 was less expressive, and on the contrary, the strain ε1 was more expressive than the samples tested, however, the thinning of the sheets as close to the tested data. Fig. 20 shows the biaxial strain for experiments A11, A13, A15, and A17, showing maximum strain data below the FFL, different from that obtained in the experimental tests, which indicates a need for correction of the FFL slope to improve the prediction of simulated failure. Fig. 21 shows the biaxial strain for experiments B11, B13, B15, B17, and B19. The maximum strains were close to or exceeded the FFL in experiments B15, B17, and B19, showing good prediction. In all simulated tests, the final sheet thickness exceeded the experimentally measured values.

Figs. 22 and 23 shows simulation images of the response to the damage evolution mechanism for both sheets. The first image from left to right is the beginning of crack nucleation or fracture, in simulation, where the first mesh element is deleted. Fig. 22 shows the failure response in experiment A17 - R4, without correction of the part radius. The failure occurred at the second-to-last step with a wall angle of 80°. Fig. 23 shows the failure response of experiment B19 - R4, without correction of the part radius. The failure occurred in the last pass at an angle of 90°. In both tests, the possible fracture was predicted, indicating that the corrections and the relationship between deformed surface area are valid for use in the MSIF study. The contour values shown in the figures represent the evolution damage on the surface of the part, presenting the most fracture-prone region.

The response to the damage evolution performed by applying the ductile damage method in Abaqus® software is presented in Fig. 24. The damage data together with thinning in experiments A17 - R4 and B19 - R4, without correction of the part radius, presented as a decreasing exponential function. In the simulated experiments, failure occurred between 0.10 mm and 0.13 mm thick. This thickness is within the bounded fracture region in experimental studies.

Although the data were of good quality for the MSIF case, with no change in the mass scale to reduce computational time, the computational time for performing the simulations using the explicit integration method is shown in Fig. 25 and is between 3.58 and 4.45 processing days. This increased computational time is related to the increased forming height, which requires a longer tool path.

In the simulations presented, it was verified that the corrections generated by the FFL and critical thickness analysis, as well as in the physical experiments provided fracture-free parts, ensuring the effectiveness of the method. However, although the failure prediction was efficient, the computational cost is high, and performing several simulations to analyze a product is unsustainable. Thus, performing experimental testing with real-time correction application and determining a forming surface ratio for the material in question can help in digitizing the various data applied to the process, being possible to relate process parameters, thickness sheet, tool path, and strain to establish the best choice for producing parts by the MSIF process.

6. Conclusions

The method applied in studies on multistep incremental forming showed that the use of a mixed feed rate ensured higher strain and the production of fracture-free parts with a tool radius of 4 mm. Based on the data and results presented, the multistep strategy with the application of

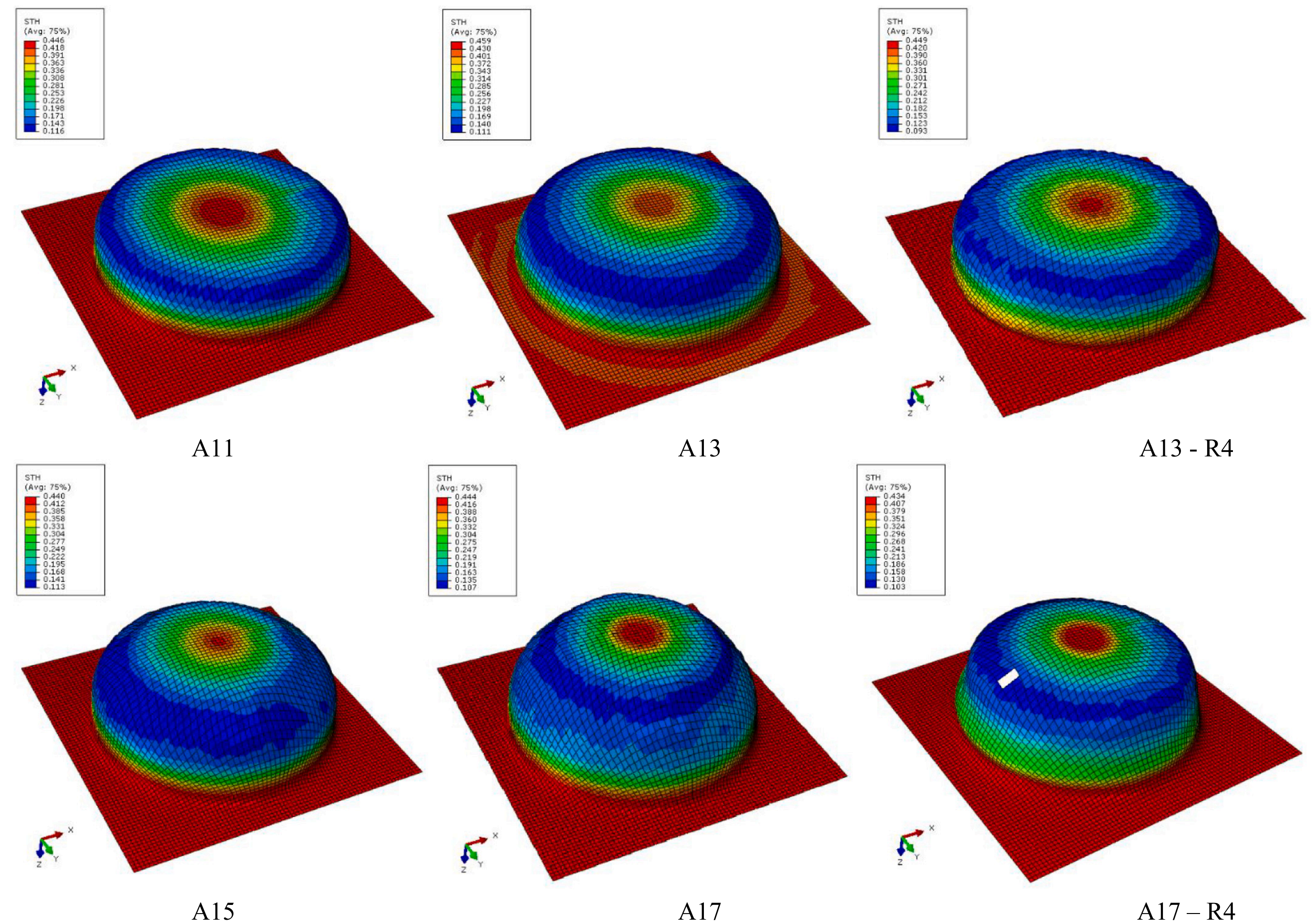

Fig. 18. Simulation of multistep incremental forming for experiments A11 to A17.

part radius correction and real-time tool path correction ensured an intact part following the procedure. The methodology use of the corrections promoted a reduction of the strain rate in the bend region of the part, which enabled a conformability gain and gain in forming height. The corrections helped to compare and establish a forming limit parameter based on the deformable surface area of the blanking and the deformed surface area of the part, for each sheet thickness, being indispensable in future research, as well as the application of computer simulation, although the computational time is still a concern. Regarding the MSIF simulation, as well as the computational model behaving like the practical experiments, the ductile damage evolution mechanism applied to the program, predicted the failure at the same forming height and wall angle, except for experiment A13. The computationally applied and simulated corrections also resulted in reduced strain rate and thinning. The simulated and experimental data also suggest that MSIF can result in lower final sheet thickness and with the application of corrections to the geometry, can generate a more uniform thickness distribution, like that found in SPIF. With the data of surface area or forming surface ratio, it is possible to assist the previous studies of the product to determine the multistep incremental forming paths, besides establishing limits for forming height and radius of the part, since these parameters are correlated.

Ethical approval

Not applicable.

Consent to participate

Not applicable.

Consent to publish

All authors read and approved the final manuscript.

Funding

Not applicable.

Availability of data and materials

The data used for this manuscript are in the work of PSOF; Experimental Study for Real Time Failure Prediction in Multipass Incremental Stamping. Doctoral Thesis. Universidade Federal do Paraná. Curitiba, 2022.

CRediT authorship contribution statement

PSOF produced, analyzed and simulated the specimens and wrote the manuscript; EFTO helped with manuscript revisions and corrections, PDV helped during the work and in the correction of the manuscript; PVPM helped during the work and in the correction of the manuscript.

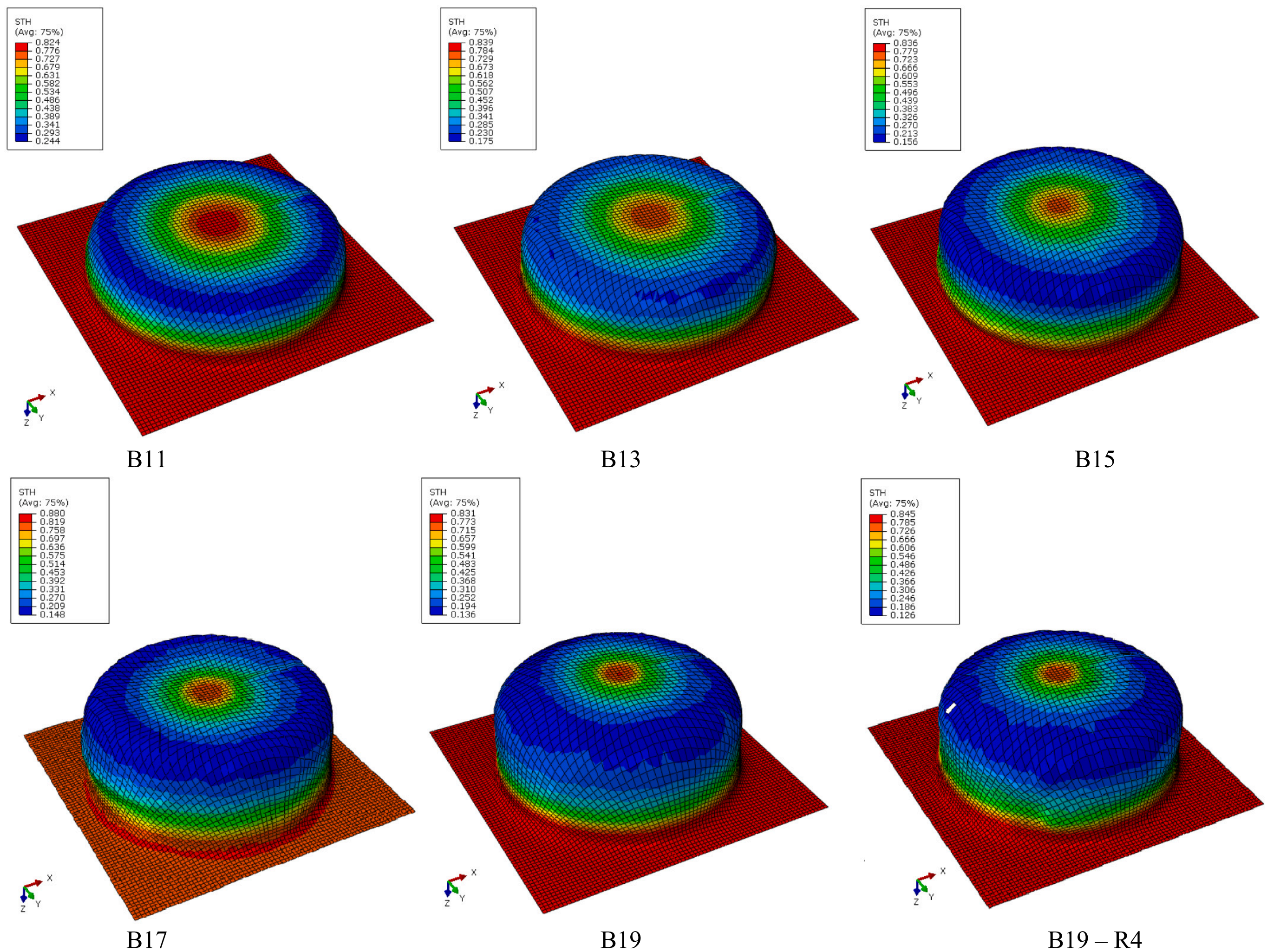

Fig. 19. Simulation of multistep incremental forming for experiments B11 to B19.

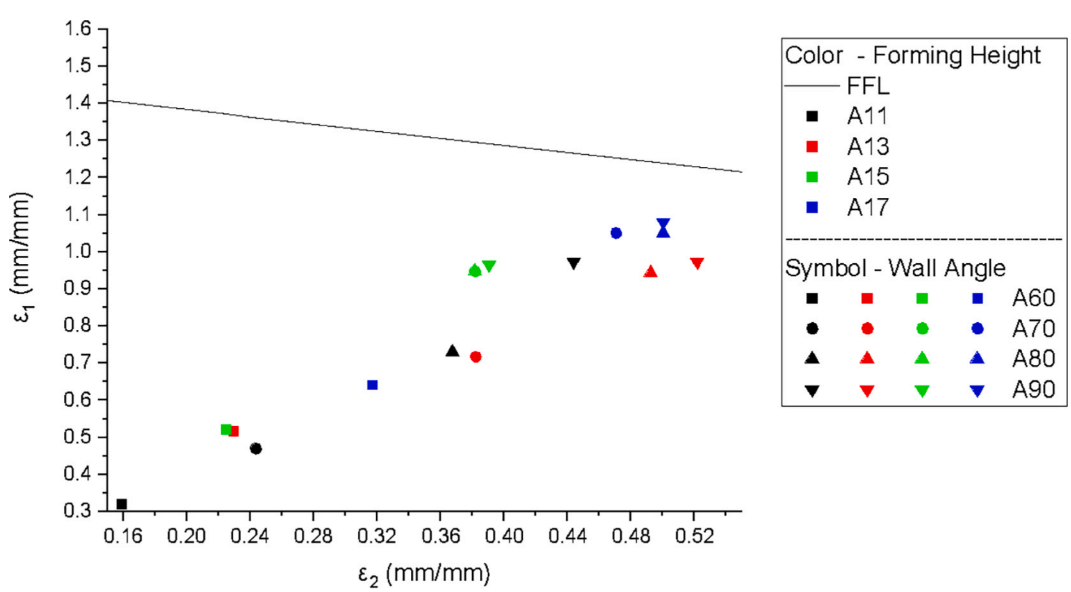

Fig. 20. Simulated biaxial strain for experiments A11 to A17.

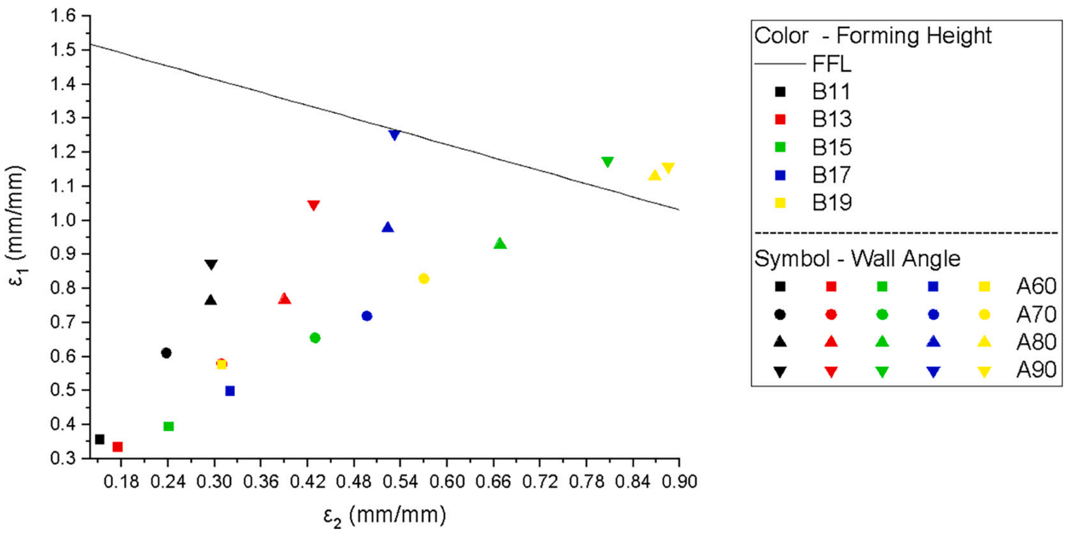

Fig. 21. Simulated biaxial strain for experiments B11 to B19.

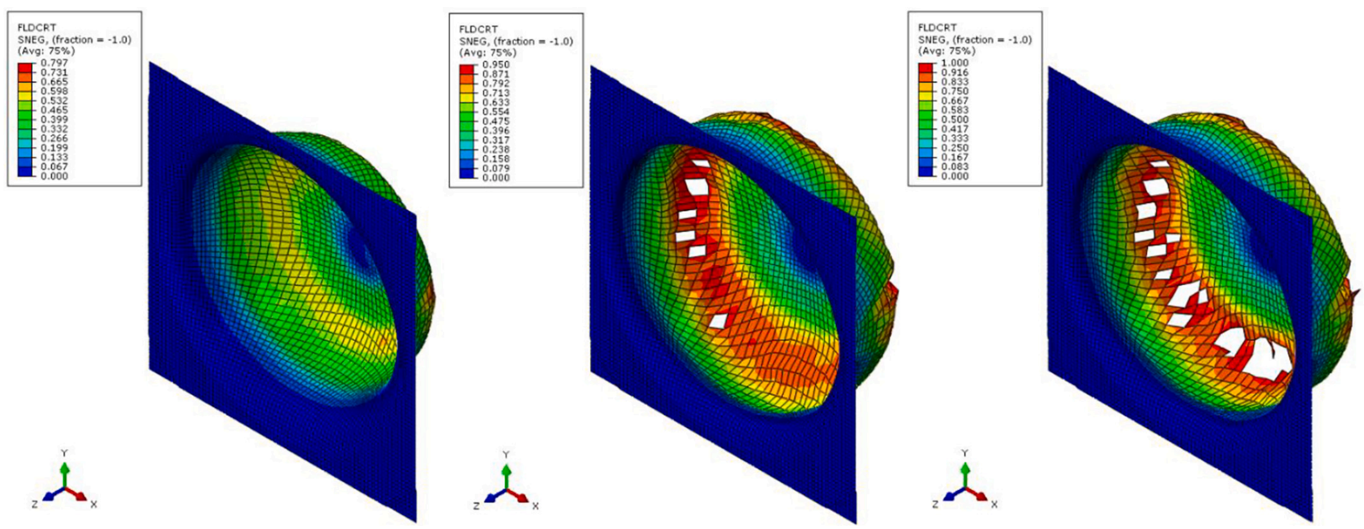

Fig. 22. Response of the damage evolution mechanism for experiment A17 - R4 without part radius correction.

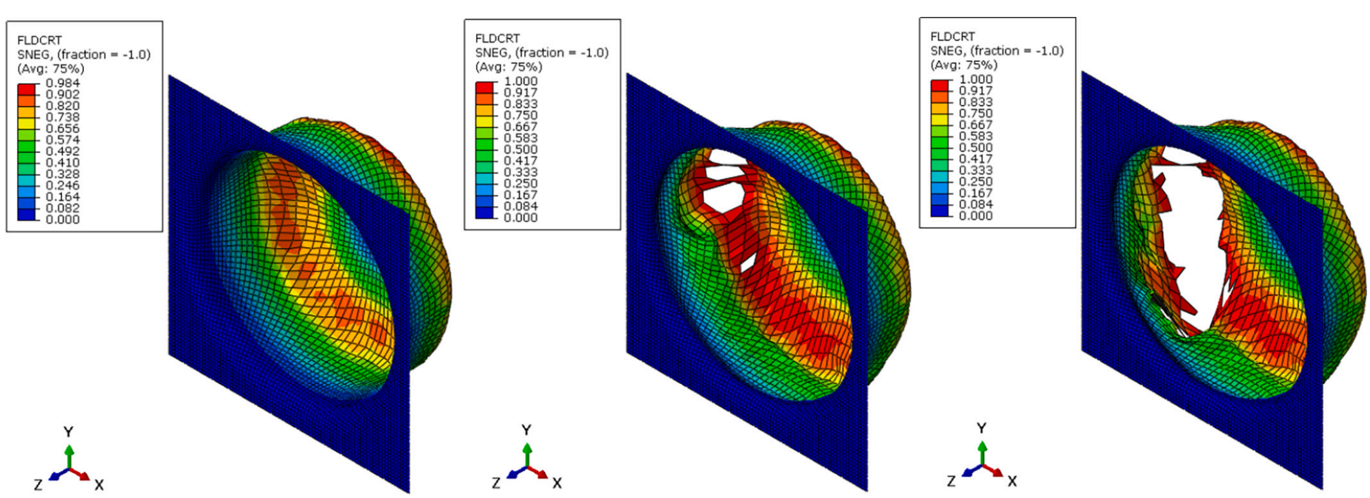

Fig. 23. Response of the damage evolution mechanism for experiment B19 - R4 without part radius correction.

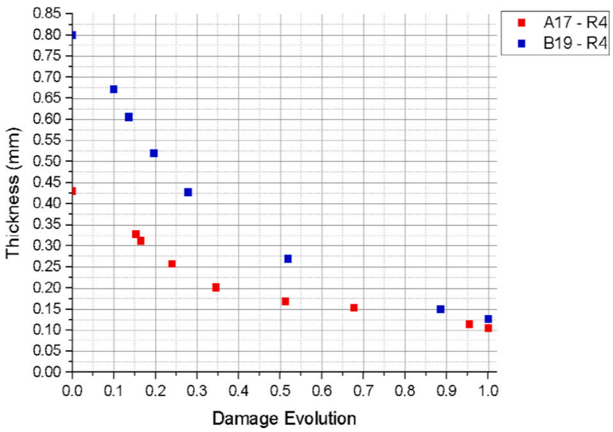

Fig. 24. Relationship between sheet thinning and damage evolution in simulated experiments in MSIF.

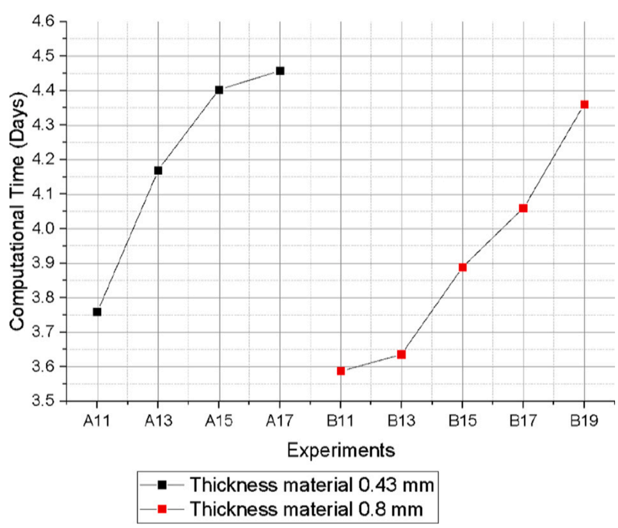

Fig. 25. Computational time in simulated experiments in MSIF.

Declaration of competing interest

The authors declare that they have no known competing financial interests or personal relationships that could have appeared to influence the work reported in this paper.

Acknowledgements

This research was supported by CNPq (Brazil).

References

[1] Ghobakhloo M. The future of manufacturing industry: a strategic roadmap toward industry 4.0. J Manuf Technol Manag 2018;29(6):910–36.
[2] Jeswiet J, et al. Asymmetric single point incremental forming of sheet metal. Ann CIRP 2005;54:623–50.
[3] Malhotra R, Xue L, Belytschko T, Cao J. Mechanics of fracture in single point incremental forming. J Mater Process Technol 2012;212(7):1573–90. https://doi.org/10.1016/j.jmatprotec.2012.02.021.
[4] Trzepieciński T, Oleksik V, Pepelnjak T, Najm SM, Paniti I, Maji K. Emerging trends in single point incremental sheet forming of lightweight metals. Metals 2021;11: 1188. https://doi.org/10.3390/met11081188.
[5] McAnulty Tegan, Jeswiet Jack, Doolan Matthew. Formability in single point incremental forming: a comparative analysis of the state of the art. CIRP J Manuf Sci Technol 2017;16:43–54. https://doi.org/10.1016/j.cirpj.2016.07.003. ISSN 1755–5817.
[6] Fischer AJ. Embodied computation: exploring roboforming for the masscustomization of architectural components. Carnegie Mellon University; 2015.
[7] Skjoedt M, Hancock MH, Bay N. Creating helical tool paths for single point incremental forming. In: Key Engineering Materials. 344. Trans Tech Publications, Ltd; 2007. p. 583–90. https://doi.org/10.4028/www.scientific.net/kem.344.583.
[8] Afonso D. Forming without a die - fundamentals and applications of single point incremental forming. Aveiro - Portugal: University of Aveiro; 2016.
[9] Afonso D, De Sousa Ricardo Alves, Pires Liliana. Incremental Forming as a Rapid Tooling Process. Switzerland: Springer Briefs in Applied Sciences and Technology; 2019.
[10] Skjoedt M, Silva MB, Martins PAF, Bay N. Strategies and limits in multi-stage single-point incremental forming. J Strain Anal Eng Des 2010;45(1):33–44. https://doi.org/10.1243/03093247JSA574.
[11] Zhang C, Xiao HF, Yu DH. Incremental forming path-generated method based on the intermediate models of bulging simulation. Int J Adv Manuf Technol 2013;67: 2837–44. https://doi.org/10.1007/s00170-012-4696-9.
[12] Malhotra Rajiv, Xue Liang, Belytschko Ted, Cao Jian. Mechanics of fracture in single point incremental forming. J Mater Process Technol 2012;212(7):1573–90.
[13] Duflou JR, et al. Process window enhancement for single point incremental forming through multi-step toolpaths. CIRP Ann. - Manuf. Technology 2008;57(1): 253–6. https://doi.org/10.1016/j.cirp.2008.03.030.
[14] Malhotra R, Bhattacharya A, Kumar A, Reddy NV, Cao JA. New methodology for multi-pass single point incremental forming with mixed toolpaths. CIRP Ann Manuf Technol 2011;60(1):323–6. https://doi.org/10.1016/j.cirp.2011.03.145.
[15] Zhaobing L, Yanle L, Meehan PA. Vertical wall formation and material flow control for incremental sheet forming by revisiting multistage deformation path strategies. Mater. Manuf. Processes 2013;28:562–71. https://doi.org/10.1080/10426914.2013.763964.
[16] Wu Song, Ma Yunwu, Gao Leitao, Zhao Yixi, Rashed Sherif, Ma Ninshu. A novel multi-step strategy of single point incremental forming for high wall angle shape. Journal of Manufacturing Processes 2020;56(Part A):697–706. https://doi.org/10.1016/j.jmapro.2020.05.009. ISSN 1526-6125.
[17] Suresh Kurra, Nasih HR, Jasti NVK, Dwivedy Maheshwar. Experimental studies in multi stage incremental forming of steel sheets. Part A Materials Today: Proceedings 2017;4(2):4116–22. https://doi.org/10.1016/j.matpr.2017.02.316. ISSN 2214-7853.
[18] Bouzid MF, Ahmed MB, Zid K, Tarchoun R. Effect of multi-stage incremental formatting strategy (DDDD) on sheet thickness and profile. In: Design and Modeling of Mechanical Systems - IV. CMSM 2019. Lecture Notes in Mechanical Engineering. Cham: Springer; 2020. https://doi.org/10.1007/978-3-030-27146-6_36.
[19] Vignesh G, Pandivelan C, Narayanan CS. Review on multi-stage incremental forming process to form vertical walled cup. Materials Today: Proceedings 2020;27 (Part 3):2297–302. https://doi.org/10.1016/j.matpr.2019.09.116. ISSN 2214-7853.
[20] Nimbalkar DH, Nandedkar VM. Review of incremental forming of sheet metal components. Int J Eng Res Appl 2013;3(5):39–51.
[21] Ablat MA, Qattawi A. Numerical simulation of sheet metal forming: a review. Int J Adv Manuf Technol 2017;89:1235–50. https://doi.org/10.1007/s00170-016-9103-5.
[22] Yamashita M, Gotoh M, Atsumi S-Y. Numerical simulation of incremental forming of sheet metal. J Mater Process Technol 2008;199(1–3):163–72.
[23] Hirtl G, Ames J, Bambach M, Kopp R. Forming strategies and process modelling for cnc incremental sheet forming. CIRP Ann Technol 2004;53:203–6.
[24] Henrard C, Bouffioux C, Eyckens P, et al. Forming forces in single point incremental forming: prediction by finite element simulations, validation and sensitivity. Comput Mech 2011;47:573–90. https://doi.org/10.1007/s00466-010-0563-4.
[25] Kurra S, Regalla SP. Analysis of formability in single point incremental forming using finite element simulations. Procedia Mater Sci 2014;6:430–5. https://doi.org/10.1016/j.mspro.2014.07.055.
[26] Malhotra R, et al. Mechanics of fracture in single point incremental forming. J Mater Process Technol 2012;212:1573–90. ISSN 7.
[27] Bharti S, Gupta A, Krishnaswamy H, Panigrahi SK, Lee MG. Evaluation of uncoupled ductile damage models for fracture prediction in incremental sheet metal forming. CIRP J Manuf Sci Technol 2022;37:499–517. https://doi.org/10.1016/j.cirpj.2022.02.023. ISSN 1755–5817.
[28] Bouhamed A, Mars J, Jrad H, Wali M, Dammak F, Torchani A, Said LB. Identification of fully coupled non-associated-ductile damage constitutive equations for thin sheet metal applications: Numerical feasibility and experimental validation. Thin-Walled Structures 2022;176:109365. https://doi.org/10.1016/j.tws.2022.109365. ISSN 0263-8231.
[29] Cao T, et al. An efficient method for thickness prediction in multi-pass incremental sheet forming. Int J Adv Manuf Technol, London 2014;77:469–83. https://doi.org/10.1007/s00170-014-6489-9.
[30] Teixeira AR, Schreiber RG, Schaeffer L. In: Influência das Velocidades de Avanço e Rotação na Estampagem Incremental de Alumínio. Centro Brasileiro de Inovação em Conformação Mecânica - CBCM - Revista Ferramental; 2018. p. 5.
[31] Radu C, et al. The effect of residual stresses on the accuracy of parts processed by SPIF. Mater Manuf Process 2013;28:572–6.
[32] Uheida EH, Oosthuizen GA, Dimitrov D. Investigating the impact of tool velocity on the process conditions in incremental forming of titanium sheets. Procedia Manuf 2017;7:345–50. https://doi.org/10.1016/j.promfg.2016.12.085.
[33] Wang J, Nair M, Zhang Y. An efficient force prediction strategy in single point incremental sheet forming. In: Elsevier - procedia manufacturing. 5; 2016. p. 761–71.
[34] Yamamura N, Kuwabara T, Makinouchi A. Springback simulations for stretchbending and drawbending processes using the static explicit FEM code, with

an algorithm for canceling non-equilibrated forces. In: Y. in Proc. 5th Int. Conf. NUMISHEET2002. Jeju Island, Korea; 2002. p. 25–30.

[35] Lajarin SF, Marcondes PVP. In the work: influence of computational parameters and nonlinear unloading behavior on springback simulation. J Braz Soc Mech Sci Eng 2013;35:123–9. https://doi.org/10.1007/s40430-013-0014-1.

[36] Cao J, et al. Experimental and numerical investigation of combined isotropic-kinematic hardening behavior of sheet metals. International Journal of Plasticity 25 (2009) 942–972, v. 25, p. 942–972, 2009. Rev. Ferrament. 2018:5.

[37] Saidi B, et al. Prediction of the friction coefficient of the incremental sheet forming SPIF. In: Proceedings of the 6th international congress design and modelling of mechanical systems CMSM, Hammamet, Tunisia; 2015.

[38] Olivio Filho PS. Avaliação Numérica da Predição de Forças no Processo de Estampagem Incremental de Ponto Único. Curitiba: UFPR; 2017. Dissertação de Mestrado.

[39] ABAQUS/Standard User's Manual Version 614. Dassault Systemes Simulia, Inc. March 3, http://130.149.89.49:2080/v6.14/; 2015.